Large-Scale Nanophotonic Solar Selective Absorbers for High-Efficiency Solar Thermal Energy Conversion

*Pengfei Li, Baoan Liu, Yizhou Ni, Kaiyang Kevin Liew, Jeff Sze, Shuo Chen, and Sheng Shen**

At present, the conversion of solar energy into electricity mainly relies on two approaches: solar photovoltaics that convert solar photons directly into electricity, and solar thermal energy conversion in which solar photons are first converted into thermal energy, then converted to electricity. Compared to traditional photovoltaics, one major advantage of solar thermal energy conversion is the utilization of nearly the entire solar spectrum, allowing for higher energy conversion efficiency. In solar thermal technologies, such as concentrated solar power,[1] solar thermophotovoltaic,[2] solar thermionic,[3] and solar thermoelectric systems,[4] solar absorbers are crucial components that absorb and convert sunlight into thermal energy. In order to achieve the maximum conversion efficiency of incident solar flux to heat, one important strategy is to employ spectrally selective solar absorbers that exhibit a near-blackbody absorption in the solar spectrum while suppressing infrared emission at elevated temperatures. However, developing cost-effective and large-scale solar selective absorbers with both high conversion efficiency and high-temperature stability remains a challenge. Here, we demonstrate metal-based wafer-scale nanophotonic solar selective absorbers with excellent solar selective absorptivity and thermal stability, using a template (mold) stripping method which can drastically increase throughput and decrease fabrication cost. The novel solar selective absorbers with 3D nanophotonic structures can significantly facilitate transformative advancements in the design and performance of solar thermal systems.

For mid- and high-temperature operations of solar thermal systems, especially concentrated solar power systems, the development of high-performance solar selective absorbers has been challenging due to a variety of factors such as spectral performance, material stability at high temperatures, and manufacturing cost. Metal–dielectric multilayer structures can achieve a good spectral selectivity because of the interference effect. However, the use of these multilayer structures in practice is limited by both high-temperature instability and high-cost fabrication such as sputter deposition and electron beam evaporation.[5,6] Semiconductor–metal structures utilize semiconductors with proper bandgaps to absorb solar radiation, and an underlying layer of metal to provide high infrared reflectance. A selective coating with Si–Ge nanoparticles has recently been demonstrated to have a measured solar absorptivity ≈90% and an infrared emissivity <30%.[7] The main drawback of the semiconductor–metal composition is the nonflexible spectral selectivity due to the intrinsic bandgaps of semiconductors. Cermet-based coatings made of ceramic–metal composites have also been developed and studied for use in solar selective absorbers. Thin single or multiple cermet layers are typically deposited on a metal surface for high solar absorptance while being transparent to infrared radiation. Although various combinations of host ceramics such as Al_2O_3, AlN, and SiO_2 with metal particle fillers including Ni, Co, Mo, W, Au, Ag, etc., have been extensively investigated in terms of spectral performance and thermal stability, it is still quite difficult to develop high-performance cermet-based absorbers stable at >700 °C.[8,9] Nanophotonic structures, e.g., 1D, 2D, and 3D photonic crystals, have been explored for use as solar selective absorbers, but these structures are far from meeting the goal of ≈100% absorptance for the broadband solar spectrum.[10–14] Moreover, these nanophotonic structures are fabricated through high-cost and complex processes, such as reactive ion etching (RIE), atomic layer deposition (ALD), chemical mechanical planarization (CMP), and cannot be easily scaled up.

An optimal solar absorber needs to maximize the solar-to-electrical energy conversion.[15] The solar-to-electrical conversion efficiency η of a solar thermal system (**Figure 1**a) can be calculated by multiplying the solar-to-thermal conversion efficiency $\eta_{\text{solar-th}}$, which is exclusively determined by the properties of the solar absorber, and the thermal-to-electrical energy conversion efficiency $\eta_{\text{th-e}}$. The theoretical maximum of $\eta_{\text{th-e}}$ is the Carnot efficiency, namely, $\eta_{\text{th-e}} = 1 - T_0/T_A$, where T_0 is the ambient temperature and T_A is the working temperature of the solar absorber. As a result, we can quantitatively characterize the performance of the solar absorber by the overall efficiency of the solar thermal system

$$\eta = \eta_{\text{solar-th}} \times \left(1 - \frac{T_0}{T_A}\right) \quad (1)$$

where $\eta_{\text{solar-th}}$ is a function of the frequency-dependent absorptivity $\alpha(\lambda)$ and the working temperature of the solar absorber.

P. Li, B. Liu, K. K. Liew, J. Sze
Department of Mechanical Engineering
Carnegie Mellon University
5000 Forbes Ave., Pittsburgh, PA 15213, USA
Y. Ni, Prof. S. Chen
Physics Department
University of Houston
4800 Calhoun Rd., Houston, TX 77004, USA
Prof. S. Shen
Department of Mechanical Engineering
Carnegie Mellon University
5000 Forbes Ave., Pittsburgh, PA 15213, USA
E-mail: sshen1@cmu.edu

DOI: 10.1002/adma.201501686

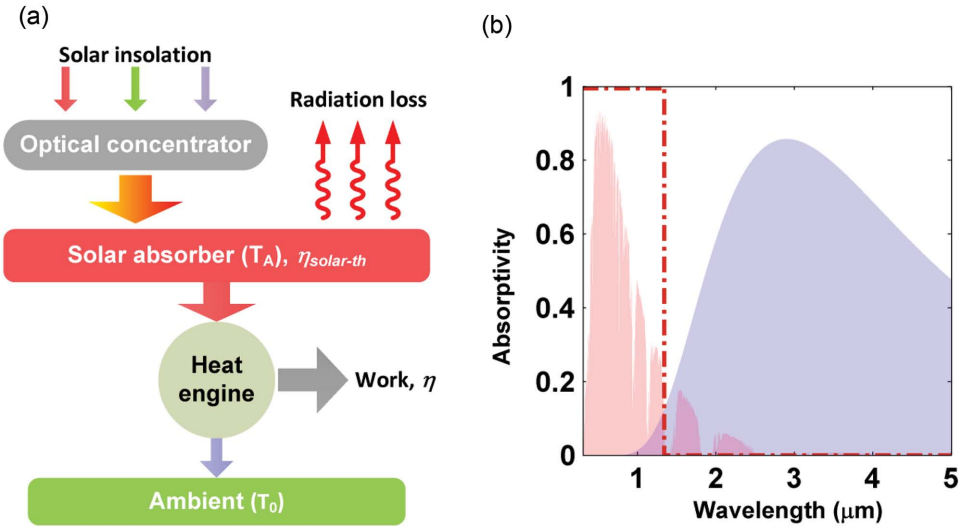

Figure 1. Solar selective absorber in a solar thermal system. a) Schematic of the solar thermal system. b) The pink and blue areas indicate the solar spectrum and the blackbody radiation spectrum at 1000 K, respectively. The red dashed line is the spectral absorptivity of an ideal solar absorber.

Based on energy balance equation, $\eta_{\text{solar-th}}$ can be explicitly expressed as[16]

$$\eta_{\text{solar-th}} = \frac{C \times \int d\lambda \cdot \alpha(\lambda) \cdot E_{\text{solar}}(\lambda) - \int d\lambda \cdot \alpha(\lambda) \cdot E_B(\lambda, T_A)}{C \times \int d\lambda \cdot E_{\text{solar}}(\lambda)} \quad (2)$$

where E_{solar} is the spectral solar irradiation, $E_B(\lambda,T_A)$ is the blackbody radiation at temperature T_A, and C is the concentration factor that is usually on the order of 10–1000. It is worth noting that if the absorber is placed in air, the convection loss through air also needs to be considered in addition to radiation loss.

Ideally, solar absorbers should have a step-function like spectral selection with 100% absorption for the solar spectrum and 0% emission for the infrared range, where the "cut-off" wavelength is located at the intersection of $C \times E_{\text{solar}}$ and E_B, as illustrated in Figure 1b. However, in reality, there exists no optical structure reaching this ideal performance. For any realistic structure, we have to consider its detailed spectral absorptivity/emissivity ($\alpha(\lambda)$) for both sunlight and thermal infrared radiation (at T_A). In Equation (1), increasing T_A leads to a higher Carnot efficiency but simultaneously reduces $\eta_{\text{solar-th}}$ due to an increasing radiation loss. Thus, for a given solar absorber, considering its specific structure (e.g., multilayer or 3D photonic crystals) and material, and the concentration factor C, we can always find its optimized geometry and working temperature T_A by maximizing the overall conversion efficiency η.

Here, we employ metal nanopyramid structures to design solar selective absorbers based on light trapping principles.[17,18] Although nanopyramid structures have been used to enhance the absorption of c-Si or GaAs solar cells in the solar spectrum above the electronic bandgaps of the semiconductors,[19–21] generally, selective solar absorption and high-temperature stability are not required for solar cells. In addition, fabrication of nanopyramid structures onto solar cells is usually expensive, and difficult to be scaled up. In this work, metals are chosen as the absorber base materials because they are usually stable at high temperatures and have a high reflectance (thus low emittance) in the infrared range. For the infrared light whose wavelength is much larger than the size of nanopyramids, the nanopyramid structure performs as a perfect reflector with reflectivity close to 100% (i.e., ≈0% emissivity). On the other hand, the nanopyramid structure behaves like a perfect solar absorber in the solar spectrum due to the tapered subwavelength geometry of the nanopyramids, which generally exhibits broadband antireflection performance. The nanopyramids can enhance solar absorption by matching the wave impedance between air and the metal substrate because the effective refractive index gradually changes from $n = 1$ at the top to $n = n_{\text{metal}}$ at the bottom.[22] To achieve an even better impedance match, a thin layer of an antireflective material, such as aluminum oxide (Al_2O_3) and silicon nitride (SiN_x), can be coated onto the nanopyramids, which increases the absorption by further mitigating the abrupt change of the effective refractive indexes at the top and bottom of the nanopyramids.

We fabricate large-scale nickel nanopyramid structures via a template stripping method,[23,24] as shown in **Figure 2**a. The entire fabrication process starts with patterning a thin silicon nitride layer on a regular (100) silicon wafer. Using laser interference lithography, nanohole arrays are patterned onto the silicon nitride layer. This layer serves as a mask for anisotropic potassium hydroxide (KOH) etching, which results in inverted nanopyramids on the silicon wafer. After the etching step, the silicon nitride layer is removed with hydrofluoric acid (HF) etching. The silicon wafer is then used as a template for rapid replication of the nanopyramids with nickel. A 100 nm thick nickel film is first sputtered on the silicon master template as a seed layer for electrochemical deposition. The replicating nickel layer can reach any desired thicknesses with electrochemical deposition. Due to water-assisted subcritical debonding between nickel and native oxide on the silicon wafer,[25–27] the nickel layer with nanopyramid arrays can be readily peeled off from the silicon master template. The facets of the resulting nickel nanopyramids are atomically smooth and free of contamination (Figure 2b inset). The stripped functional sheet can

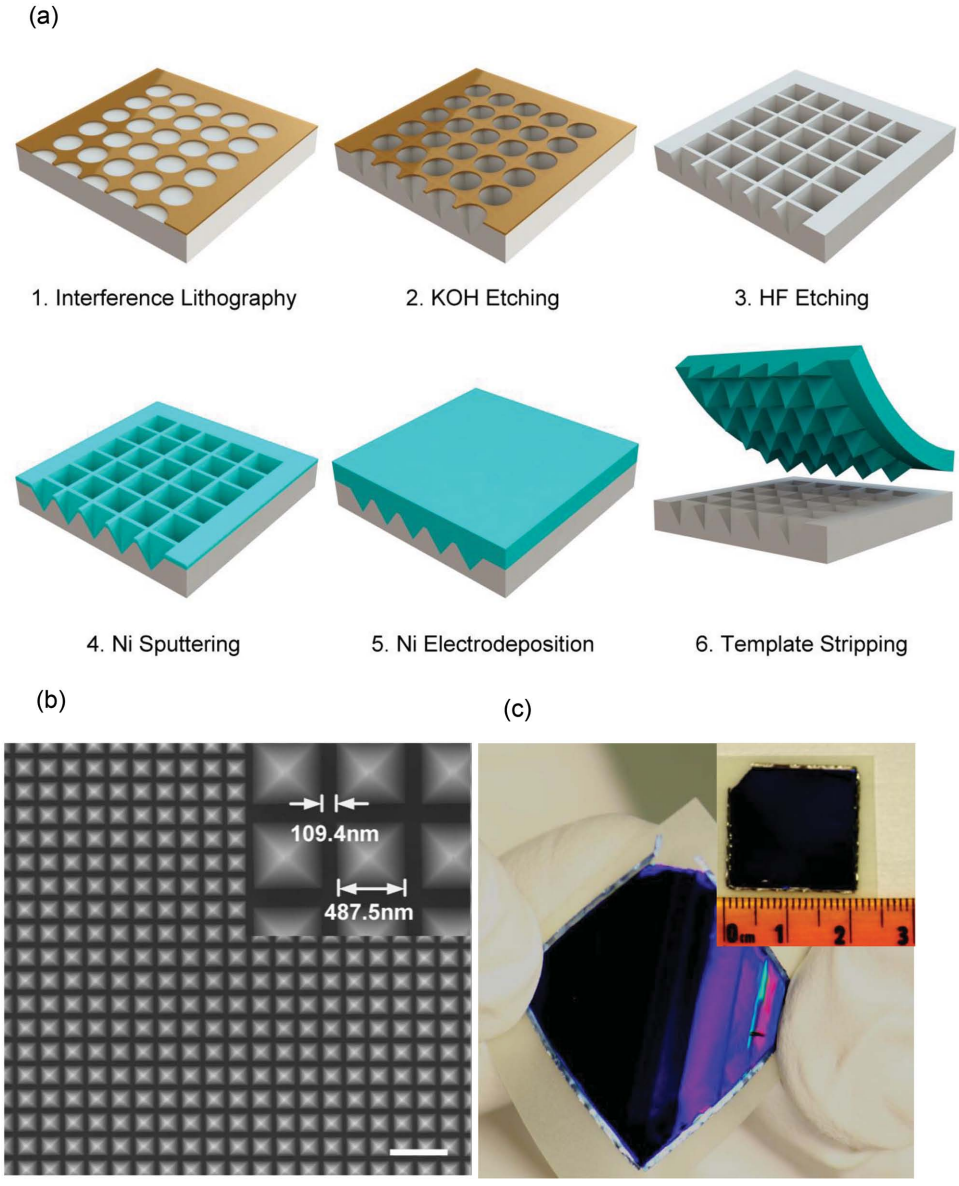

Figure 2. Fabrication of nanopyramid arrays as a solar selective absorber. a) Fabrication flow of the solar selective absorber. b) SEM images of the fabricated nanopyramid structures. Scale bar: 3 μm. c) A photograph of the flexible solar absorber.

be attached to either flexible or rigid substrates of various materials depending on their target applications (Figure 2c). Compared with the previous works using nanophotonic structures as selective surfaces, the large-scale nanofabrication process developed here is particularly cost-effective and robust because a variety of low-cost metals such as nickel, copper, and their alloys can be used. After the peeling step, the silicon templates or molds retain their original conditions with little contamination or damage. Therefore, they can be reused many times, leading to a low-cost and high-throughput fabrication process.

In order to maximize the energy conversion efficiency η, we apply the aforementioned universal principle (Equations (1) and (2) to optimize the design of nickel nanopyramid structures as solar selective absorbers. **Figure 3**a shows the schematic of nickel nanopyramid arrays. The shapes of all the pyramids are uniquely determined by the KOH etching of the (100) silicon wafer, where the angle equals 54.7°. The selective absorption of nickel nanopyramid arrays is determined by the following parameters: (1) length of the pyramid edge l; (2) distance between adjacent pyramids d; and (3) thickness of the antireflection coating (ARC) h, all of which can be tuned in our fabrication process. We numerically search the best design by maximizing η from all the possible cases with different combinations of l, d, and h. For each case, we first perform direct numerical simulation to obtain the spectral absorptivity $\alpha(\lambda)$. Then, the maximum overall efficiency η_m for this case is solved together with the optimized working temperature T_A based on Equations (1) and (2). As a result, the best design of nickel nanopyramid arrays is determined by the case where η_m reaches a global maximum.

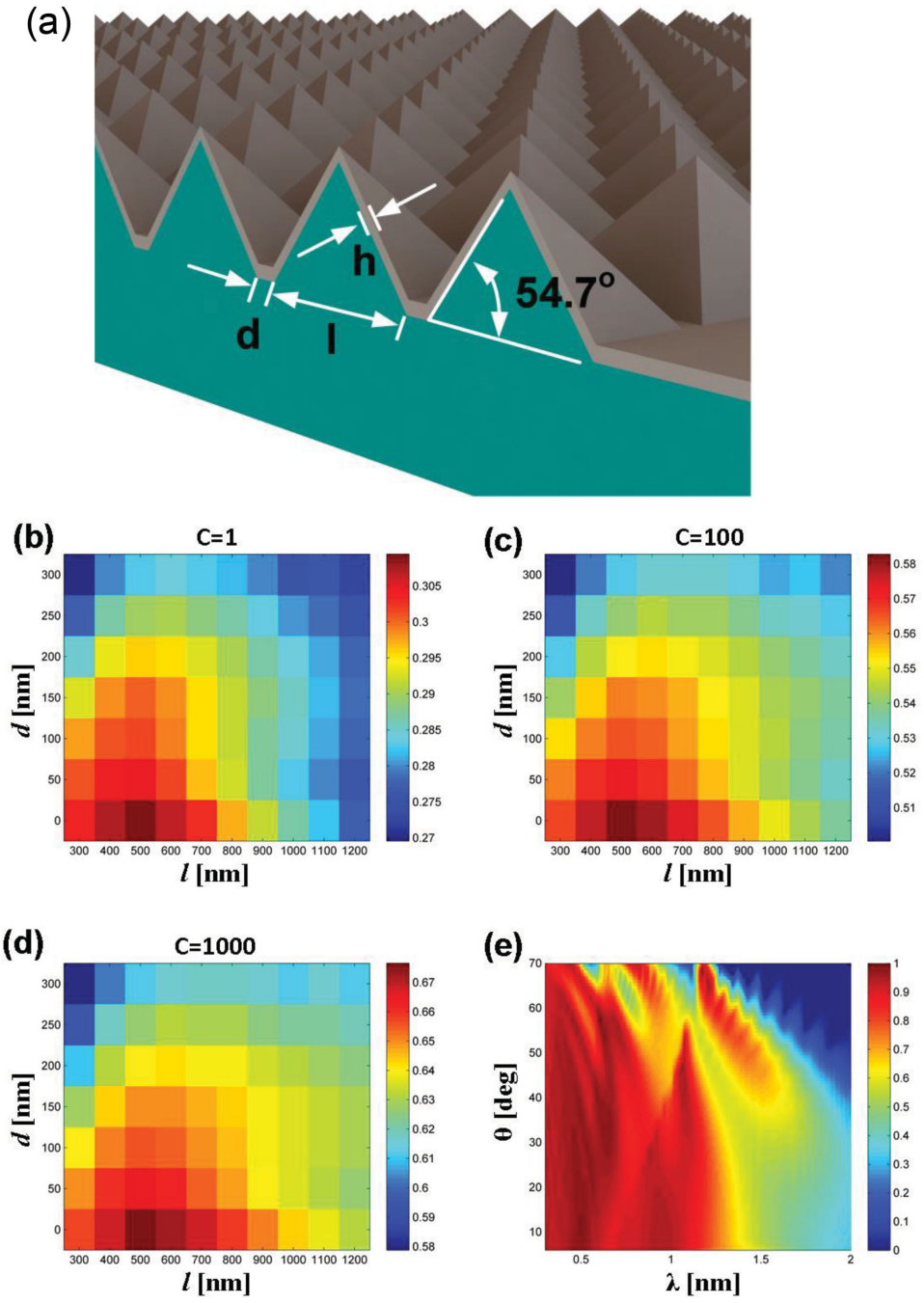

Figure 3. Optimization of solar absorber geometries. a) Schematic of nickel nanopyramid arrays with an ARC layer. Maximized overall efficiencies at concentration factors: b) $C = 1$, c) $C = 100$, and d) $C = 1000$. e) Averaged absorptivity spectrum at different incident angles θ for $l = 500$ nm, $d = 100$ nm, and $h = 75$ nm.

According to the numerical search results (Figure 3), the optimized design of the nickel nanopyramid arrays as selective solar absorbers needs to satisfy the following three criteria: (1) the length of pyramid edge l is about 500 nm; (2) the distance between adjacent pyramids d should be as small as possible; and (3) the thickness of the antireflection coating h is around 70 nm as long as the pyramidal shapes are preserved after coating the pyramids with Al_2O_3. For the third criterion, we want to emphasize that the antireflection coatings with thickness $h \in$ [70 nm, 300 nm] achieve very similar performance (see the Supporting Information). However, we choose $h \approx 75$ nm as the optimal design in order to lower fabrication cost. Furthermore, thick Al_2O_3 coatings will increase the thermal emission in the infrared range due to its optical phonon resonance. While our numerical search is based on solar concentration factor $C = 1$, it turns out that the optimal design is insensitive to the variation

of C. Figure 3b–d illustrates the maximized overall efficiency η_m for different combination of l and d at $h = 75$ nm, for $C = 1$, 100, 1000, respectively. The optimal dimensions for different C remain almost the same. For $C = 1000$, $T_A = 1000$ °C, the theoretical overall conversion efficiency η_m with the optimized nanopyramid structures can be as large as 68%.

We also investigate the angular dependency of the absorption spectrum of nickel nanopyramid arrays. For the case of $l = 500$ nm, $d = 100$ nm, and $h = 75$ nm, we numerically evaluate the averaged absorptivity spectrum (the average of s-polarization and p-polarization contributions) for the incident angle θ up to 70° (Figure 3e). The result shows that the selective absorption maintains almost the same for the angles in the range of ±50°, which indicates the omnidirectional absorption of the nickel nanopyramid arrays.

To characterize the selective absorption properties of the functional nickel sheet, we use two spectral measurement systems to cover the visible and infrared spectra with corresponding wavelength ranging from 300 nm to 10 μm. A Perkin Elmer LAMBDA 950 UV–vis–NIR Spectrophotometer with a 150 mm diameter integrating sphere is used to measure the total absorptivity spectrum in the visible and near-infrared range. For the mid-infrared absorption measurement, a Thermo Scientific Nicolet iS50R FT-IR spectrometer is used with a gold mirror as a reference. Because the samples are all opaque to the electromagnetic waves in the aforementioned visible and infrared spectra, we simply obtain the absorptivity ($A = 1 - R$) of the samples by subtracting the measured reflectance (R). The spectral selective absorptance of the functional nickel sheets are shown in **Figure 4** with the spectrum spanning from visible to infrared range. We have measured two types of samples, one type has a nanopyramid pitch size of 800 nm ("P800"), the other type has a pitch size of 600 nm ("P600"). The P800 and P600 samples have base widths $l = 600 \pm 50$ nm and $l = 500 \pm 30$ nm, respectively. The thicknesses of Al_2O_3 ARC coatings are ≈75 nm for both cases. The finite-difference time domain (FDTD) simulated absorptivity of the nickel nanopyramid structures agrees well with our measurements (Figure 4a). As shown in Figure 4b, the absorption of bare nickel nanopyramids can be further enhanced by adding the ARC layer. The nanopyramids arrays with ARC layer are intrinsically complex. The small bumps and dips observed in their absorption spectrum may be caused by the combined photonic phenomena, such as interference, plasmonics, and resonance, and the system errors of measurement instruments. The spectral absorptance of the functional nickel sheet clearly shows a highly selective characteristic over the measurement range. For the wavelength below about 1.3 μm, the average absorptance is ≈0.95, which is almost twofold higher than that of a flat nickel surface (Figure 4b). Beyond a narrow transition range from 1 to 2.5 μm, the absorptance of the nickel sheet falls to a value as low as 0.1 for wavelengths >2.5 μm, which is remarkably beneficial for the low thermal emission in the infrared range.

The stability of solar selective absorbers at high operating temperatures is of great importance for their practical application. A thermal annealing test is conducted using the samples fabricated with the aforementioned process. The fabricated solar absorbers are annealed at a temperature of 800 °C in vacuum (<1.5×10^{-5} Torr) for 5 h. The spectral absorptance

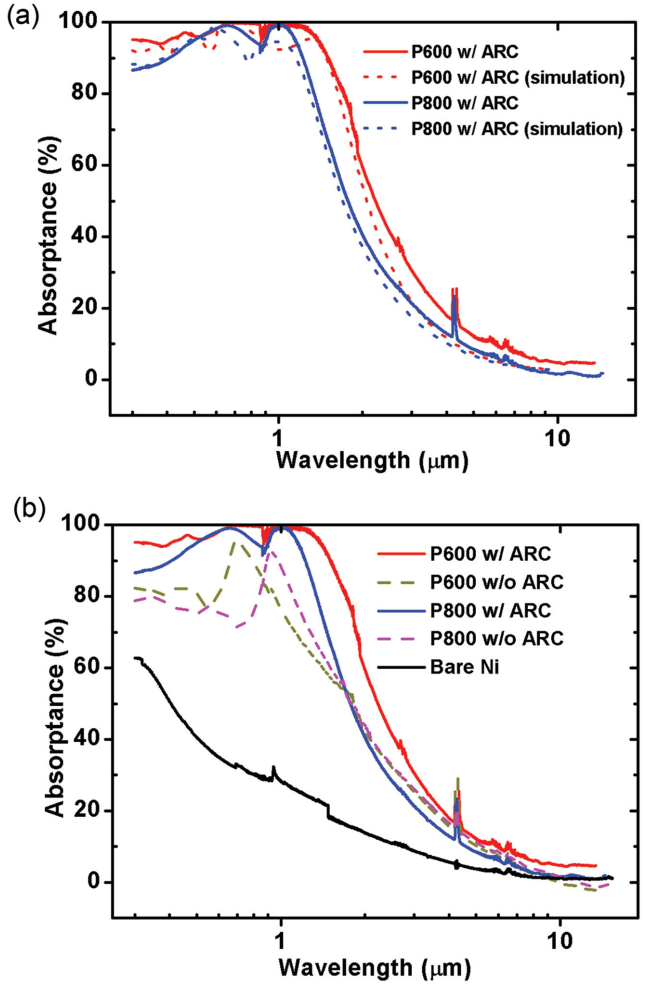

Figure 4. Spectral absorptance of nanophotonic solar selective absorbers. a) Spectral absorptance from both experiment and simulation. The solid curves are the measured results from experiments, and the dashed curves are from simulations. b) Measured spectral absorptance for a bare nickel plate, P600 sample with/without ARC, and P800 sample with/without ARC.

after annealing is slightly degraded compared to the original samples (**Figure 5**a). In the wavelength range between 500 nm and 1 μm, an ≈8% drop in absorption is observed, whereas an ≈10% increase in absorption is in the infrared range (5–15 μm). This is probably due to phase transition or crystal growth during the annealing process which causes a slight change in the surface topography, or the oxidation of nickel in the medium high vacuum for annealing. Further investigation using scanning electron microscopy shows that the surface of nanopyramids becomes rougher after annealing, but the overall nanopyramid structures are still well maintained, as shown in Figure 5b. The thermal stability test demonstrates that the nickel nanopyramids based solar absorbers have great potential for high-temperature applications. However, the long-term (e.g., years) high-temperature stability of the solar absorbers is still unknown at present, and needs further tests including thermal cycling.

In summary, we have developed large-scale low-cost nanophotonic solar absorbers based on nickel nanopyramid

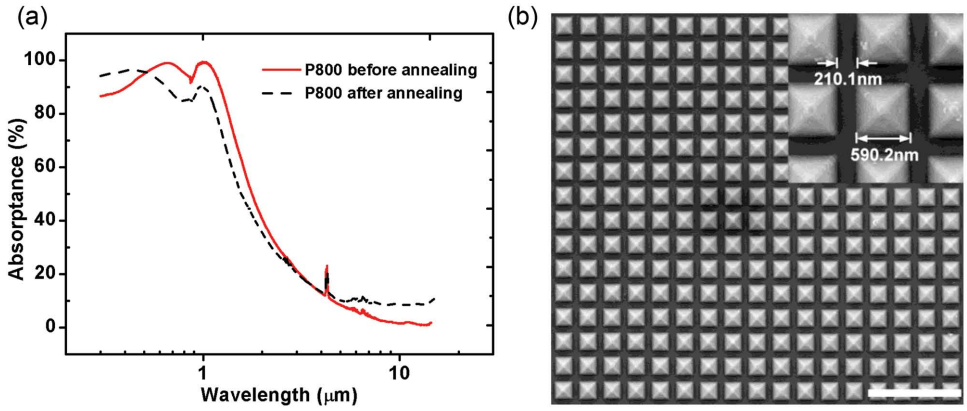

Figure 5. Thermal stability test at high temperature. a) Solar selective absorptance before (solid curve) and after 800 °C annealing in vacuum for 5 h (dashed curve). b) SEM image of the nanoprymid arrays after 800 °C annealing. Scale bar: 3 μm.

structures. Our fabrication process mainly exploits cost-effective materials and technologies such as template stripping and electroplating. The theoretical solar-to-electricity energy efficiency of the solar absorbers can be as large as 68% at the solar concentration of 1000. The measured absorptivity/emissivity demonstrates excellent spectrum selection with ≈95% solar absorptivity and ≈10% emissivity in the infrared range. Due to the 3D design, the excellent selective absorption maintains for the incident angles in the range of ±50°, which indicates the omnidirectional absorption of the solar absorbers. The thermal annealing tests indicate that the nickel nanophotonic absorbers are stable at 800 °C. The combined spectrum selection, high-temperature stability, and omnidirectional absorption demonstrated in our work are unprecedented compared to existing solar absorber structures/materials. Other than solar-to-electricity energy conversion, the high-performance solar selective absorbers can be equally applied to other solar thermal systems, such as solar water heaters and solar fuel production.

Experimental Section

Fabrication of Nickel Nanopyramids Based Solar Selective Absorbers: The original silicon wafer had a silicon nitride layer with a thickness of 50 nm, after the lithography and further HF etching, nanohole arrays were patterned onto the silicon nitride layer. This layer served as a mask layer for anisotropic KOH wet etching of the exposed area of the silicon wafer. Due to a large difference in the etching rates of (111) and (100) planes, inverted nanopyramids were therefore formed on the silicon wafer after the wet etching. This silicon wafer was then used as a template for rapid replication of the nanopyramids with nickel. To perform the nanopyramid replication, the silicon master template was sputtered with a 100 nm layer of nickel. The sputtered nickel served as a seed layer for nickel electroplating. With the electrochemical deposition step, the nickel layer can reach any desired thickness. This electroplated nickel layer not only supplied a mechanical support for nanopyramid replication, but also facilitated the nickel stripping. After the electrochemical deposition, the whole assembly was subjected to deionized water immersion. Due to the water-assisted debonding, a crack front of the nickel and silicon master template rapidly grew throughout the nickel–silicon interface when an external peeling force was applied. Consequently, a perfect nickel replication of nanopyramid structures was obtained. After peeling off the nickel layer, the template or mold can be reused many times, leading to a low-cost and high-throughput process. In order to further enhance the solar absorptance of the absorber, an ≈75 nm thick Al_2O_3 ARC layer was sputtered on top of the nanopyramids.

Numerical Simulation of Nickel Nanopyramid Structures: The FDTD method was used to simulate the absorptivity spectrum of all the possible structures (l, d, h) by using Lumerical FDTD Solutions. Considering the precision and constraints of the fabrication techniques, the length of the pyramid edge l was enumerated from 300 to 1200 nm with an increment of 100 nm. The pyramid-to-pyramid distance d was enumerated from 0 to 300 nm with an increment of 50 nm. The thickness of antireflection coating h was enumerated from 0 to 300 nm with an increment of 25 nm. In addition, Al_2O_3 was chosen as the material of the ARC layer in the simulations. After their absorptivity spectra were obtained, the maximal overall efficiency η_m and the optimal working temperature T_A for each case were numerically solved based on Equations (1) and (2) using MATLAB.

Absorption Measurements: The Perkin Elmer LAMBDA 950 UV–vis–NIR Spectrophotometer is equipped with a Hamamatsu R-955 photomultiplier tube (PMT) detector and a thermoelectrically cooled lead sulfide (PbS) detector together covering a wavelength range from 300 to 2500 nm, which includes both the visible and near-infrared spectra. With this system, the total reflectance spectra of the functional nickel sheet could be measured, with both specular and diffusive reflection included. A beam size about 5 mm in diameter was chosen which was large enough to fully reveal the surface reflection properties and compensate for the surface nonuniformity due to the fabrication process. The angle of the incidence beam was 8° with reference to the sample surface normal, which is a default in this spectrometer. However, with a sample center mounted in the integrating sphere, the total reflections can be characterized at various incident angles. Before measurements, a calibration standard made of Spectralon was used which has a high reflectance and Lambertian behavior. Using the Thermo Scientific Nicolet iS50R FT-IR spectrometer, the infrared spectrum for reflection measurements can be extended from 2500 to 15 000 nm with a liquid nitrogen cooled mercury cadmium telluride (MCT) detector. The lens for the FT-IR microscope used was a 15× infinity corrected reflachromat objective with a numerical aperture of 0.58. The angle of incident beam of the infrared source was 0° to the surface normal of the measured sample. A gold mirror was used as a reference with known specular reflectance.

Thermal Stability Tests: The thermal stability tests were carried out in vacuum. Each sheet was first sealed in a 1 in. diameter quartz tube, where the pressure was below 1.5×10^{-5} Torr. Then each tube was heated in a tube furnace (Lindberg/Blue M) with a heating rate of 22.2 °C min^{-1} till the desired temperature (800 °C), where the temperature was held for >5 h. After the furnace was naturally cooled down to room temperature, the quartz tube was removed and carefully broken to obtain the sample for further tests.

Supporting Information

Supporting Information is available from the Wiley Online Library or from the author.

Acknowledgements

This work was supported by the US National Science Foundation (NSF) Grant No. CBET-1253692 for thermal radiation measurements and seed grant from the Wilton E. Scott Institute for Energy Innovation at Carnegie Mellon University for sample fabrication.

Received: April 9, 2015
Revised: June 5, 2015
Published online: July 2, 2015

[1] *Concentrating Solar Power Technology: Principles, Developments and Applications* (Eds: K. Lovegrove, W. Stein), Woodhead Publishing Limited, Philadelphia, PA **2012**.
[2] A. Lenert, D. M. Bierman, Y. Nam, W. R. Chan, I. Celanović, M. Soljačić, E. N. Wang, *Nat. Nanotechnol.* **2014**, *9*, 1.
[3] J. W. Schwede, I. Bargatin, D. C. Riley, B. E. Hardin, S. J. Rosenthal, Y. Sun, F. Schmitt, P. Pianetta, R. T. Howe, Z.-X. Shen, N. A. Melosh, *Nat. Mater.* **2010**, *9*, 762.
[4] D. Kraemer, B. Poudel, H.-P. Feng, J. C. Caylor, B. Yu, X. Yan, Y. Ma, X. Wang, D. Wang, A. Muto, K. McEnaney, M. Chiesa, Z. Ren, G. Chen, *Nat. Mater.* **2011**, *10*, 532.
[5] D. D. Allred, M. R. Jacobson, E. E. Chain, *Sol. Energy Mater.* **1985**, *12*, 87.
[6] J. A. Thornton, J. L. Lamb, *Thin Solid Films* **1982**, *96*, 175.
[7] J. Moon, D. Lu, B. VanSaders, T. K. Kim, S. D. Kong, S. Jin, R. Chen, Z. Liu, *Nano Energy* **2014**, *8*, 238.
[8] F. Cao, K. McEnaney, G. Chen, Z. Ren, *Energy Environ. Sci.* **2014**, *7*, 1615.
[9] F. Cao, D. Kraemer, T. Sun, Y. Lan, G. Chen, Z. Ren, *Adv. Energy Mater.* **2015**, *5*, 1.
[10] Y. X. Yeng, M. Ghebrebrhan, P. Bermel, W. R. Chan, J. D. Joannopoulos, M. Soljacic, I. Celanovic, *Proc. Natl. Acad. Sci. USA* **2012**, *109*, 2280.
[11] K. A. Arpin, M. D. Losego, A. N. Cloud, H. Ning, J. Mallek, N. P. Sergeant, L. Zhu, Z. Yu, B. Kalanyan, G. N. Parsons, G. S. Girolami, J. R. Abelson, S. Fan, P. V Braun, *Nat. Commun.* **2013**, *4*, 2630.
[12] J. G. Fleming, S. Y. Lin, I. El-Kady, R. Biswas, K. M. Ho, *Nature* **2002**, *417*, 52.
[13] V. Rinnerbauer, A. Lenert, D. M. Bierman, Y. X. Yeng, W. R. Chan, R. D. Geil, J. J. Senkevich, J. D. Joannopoulos, E. N. Wang, M. Soljačić, I. Celanovic, *Adv. Energy Mater.* **2014**, *1*.
[14] J. B. Chou, Y. X. Yeng, Y. E. Lee, A. Lenert, V. Rinnerbauer, I. Celanovic, M. Soljačić, N. X. Fang, E. N. Wang, S.-G. Kim, *Adv. Mater.* **2014**, *26*, 8041.
[15] Y. Nam, Y. X. Yeng, A. Lenert, P. Bermel, I. Celanovic, M. Soljačić, E. N. Wang, *Sol. Energy Mater. Sol. Cells* **2014**, *122*, 287.
[16] J. A. Duffie, W. A. Beckman, *Solar Engineering of Thermal Processes*, Wiley, Hoboken, NJ **2013**.
[17] L. Zhou, X. Yu, J. Zhu, *Nano Lett.* **2014**, *14*, 1093.
[18] J. Zhu, C. M. Hsu, Z. Yu, S. Fan, Y. Cui, *Nano Lett.* **2010**, *10*, 1979.
[19] G. Li, H. Li, J. Y. L. Ho, M. Wong, H. S. Kwok, *Nano Lett.* **2014**, *14*, 2563.
[20] D. Liang, Y. Huo, Y. Kang, K. X. Wang, A. Gu, M. Tan, Z. Yu, S. Li, J. Jia, X. Bao, S. Wang, Y. Yao, H. S. P. Wong, S. Fan, Y. Cui, J. S. Harris, *Adv. Energy Mater.* **2012**, *2*, 1254.
[21] A. Mavrokefalos, S. E. Han, S. Yerci, M. S. Branham, G. Chen, *Nano Lett.* **2012**, *12*, 2792.
[22] E. Rephaeli, S. Fan, *Opt. Express* **2009**, *17*, 15145.
[23] J. H. Park, P. Nagpal, K. M. McPeak, N. C. Lindquist, S. H. Oh, D. J. Norris, *ACS Appl. Mater. Interfaces* **2013**, *5*, 9701.
[24] P. Nagpal, N. C. Lindquist, S.-H. Oh, D. J. Norris, *Science* **2009**, *325*, 594.
[25] C. H. Lee, J.-H. Kim, C. Zou, I. S. Cho, J. M. Weisse, W. Nemeth, Q. Wang, A. C. T. van Duin, T.-S. Kim, X. Zheng, *Sci. Rep.* **2013**, *3*, 2917.
[26] C. H. Lee, D. R. Kim, I. S. Cho, N. William, Q. Wang, X. Zheng, *Sci. Rep.* **2012**, *2*, 1000.
[27] C. H. Lee, D. R. Kim, X. Zheng, *ACS Nano* **2014**, 8746.